

Ionic Blockades Control the Efficiency of Energy Recovery in Forward Bias Bipolar Membranes

Wei Lun Toh,[‡] Hieu Q. Dinh,[‡] An T. Chu, Ethan, R. Sauvé, Yogesh Surendranath*

[‡]These authors contributed equally.

Department of Chemistry, Massachusetts Institute of Technology, Cambridge, MA 02139,
USA

*Correspondence: yogi@mit.edu

Abstract

Limited understanding exists about the operation of bipolar membranes (BPMs) in forward bias to convert protonic gradients into electrical work, despite its emerging role in many electrochemical devices. In these device contexts, the BPM is typically exposed to complex electrolyte mixtures, but their impact on polarization remains poorly understood. Herein, we develop a mechanistic model explaining the forward bias polarization behavior of BPMs in mixed electrolytes with different acidities/basicities. This model invokes that weak acids/bases accumulate in the BPM and impose an ionic blockade that inhibits the recombination of stronger acids/bases, resulting in a substantial neutralization overpotential. We demonstrate the utility of our model to fuel cells and redox flow batteries, and introduce two materials design strategies for mitigating this inhibition. Lastly, we apply our findings to enhance the energy efficiency of carbonate management in CO₂ electrolyzers. This work highlights how non-equilibrium local environments at membrane-membrane interfaces can define the efficiency of protonic-to-electrical energy conversion.

Keywords

bipolar membranes, weak electrolytes, buffers, forward bias polarization, ionic blockade, neutralization overpotential

Introduction

The interconversion of chemical and electrical potential energy gradients underpins the function of electrochemical energy technologies.¹ Typically, this interconversion is mediated by charge transfer reactions at electrode-electrolyte interfaces.² However, electrical energy can also be converted into chemical energy in solution, via the formation of ion gradients across membrane-electrolyte interfaces.³ This mode of energy conversion is key to ion separations and electrodialysis and can be used to enhance the efficiency, selectivity, and durability of flow batteries, fuel cells, and electrolyzers.³ Thus, mechanistic understanding of ion transfer processes across membrane-electrolyte interfaces is critical for addressing frontier challenges in energy and sustainability.

Bipolar membranes (BPMs) are an emerging electrochemical technology that enables the interconversion of protonic free energy gradients in solution into electrical potential gradients.⁴⁻⁸ This capability arises from their unique structure comprising a cation exchange membrane (CEM) laminated onto an anion exchange membrane (AEM), giving rise to the

property of ionic current rectification and allowing the maintenance of a stable pH gradient between the catholyte and the anolyte.⁴⁻⁸ BPMs can be operated in both reverse and forward bias modes. In reverse bias, an applied potential drives the dissociation of water or other proton donors into charged acid and base species.^{5,6,9,10} This mode transduces electrical work into a chemical protonic gradient, and allows the continuous generation of acid and base. As a result, it has been extensively studied and applied to water electrolyzers,¹¹⁻¹⁶ CO₂ electrolyzers,¹⁷⁻²⁴ and bipolar membrane electrodialysis (BPMED) cells.^{25,26} In contrast, in forward bias, the spontaneous recombination of charged acids and bases at the bipolar junction is employed to generate a potential difference that can be used to drive electrical work in an external circuit.²⁷⁻³⁰ Consequently, this mode of operation transduces a proton gradient into electrical potential, which can be used to reduce the overall voltage of an electrolytic cell or increase the overall voltage of a galvanic cell. Indeed, forward bias BPMs have been applied to access larger cell voltages in redox flow batteries.²⁹⁻³¹ The foregoing examples showcase the opportunities BPMs offer for interconverting protonic and electrical energy.

Despite its immense potential, there is limited understanding of the factors that control the efficiency of protonic to electrical energy conversion under forward bias polarization. Existing BPM studies have predominantly examined the reverse bias mode,⁵ and the studies on forward bias have largely examined the recombination of only binary electrolytes (i.e. containing only one type of cation and one type of anion), commonly hydronium and hydroxide (**Figure 1**),³²⁻³⁴ with only a few reports investigating the effect of salt and buffer ions.^{10,33,35} To our knowledge, there have been no systematic studies of BPMs in electrolyte mixtures that contain two or more species of different acidities and basicities. This is despite the prevalence of mixed electrolytes in variety of device contexts. For example, in H₂ fuel cells and CO₂ electrolyzers, in addition to hydroxide ions, (bi)carbonates invariably co-exist as a result of CO₂ absorption.³⁶ In addition, in CO₂ electrolyzers, weak organic bases such as acetate and formate can be produced as liquid products of CO₂ reduction.³⁷ This knowledge gap of how mixed electrolytes affect the speciation and polarization behavior within forward bias BPMs severely hampers the utilization of this bias mode in complex electrolyte environments.

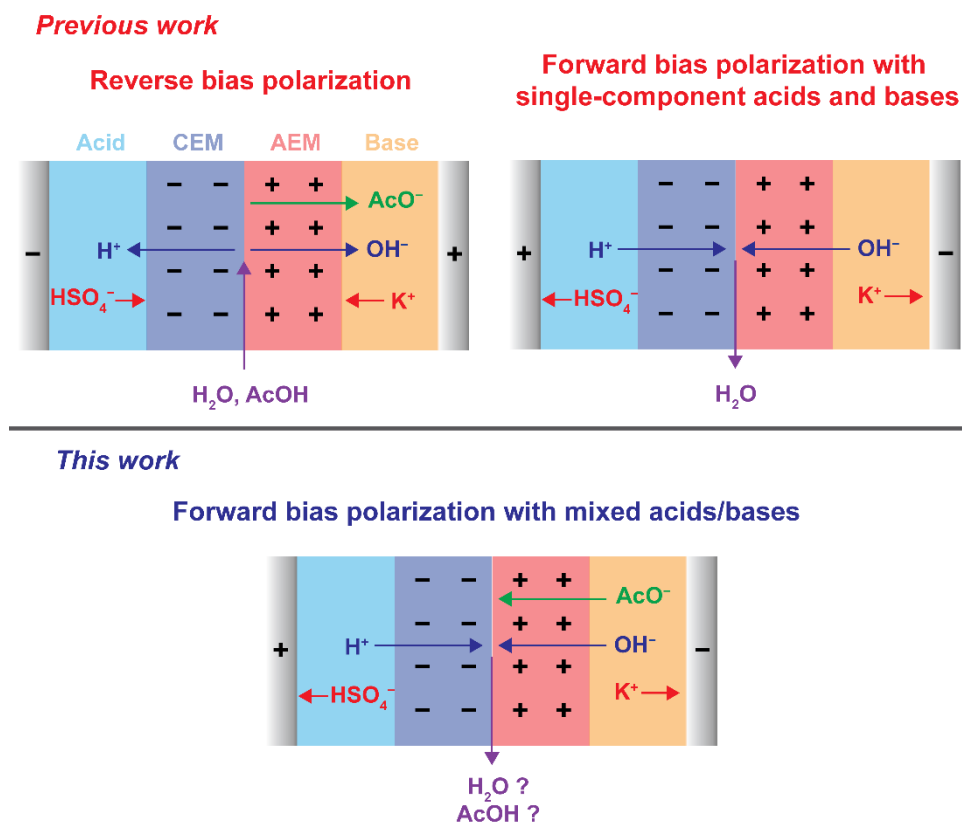


Figure 1. BPM cells operating in reverse bias and in forward bias with single-component acids and bases have been extensively studied, but the behaviour of a forward bias cell containing mixed acids or bases is poorly understood.

Herein, we develop a mechanistic model to explain the forward bias polarization behavior of a BPMs in the presence of mixed electrolytes. We show that each constituent in the mixture undergoes neutralization at a distinct membrane voltage dictated by its pK_a . Critically, we find that the presence of even a minority concentration of weak acids/bases can impose a large overpotential for the neutralization of stronger acids/bases. We show that this *neutralization overpotential* manifests in a potential-independent limiting current for forward bias operation, and results from an ionic blockade imposed by the accumulation of unreactive weak acid/base ions in the BPM. We demonstrate the utility of this model in the context of fuel cells and redox flow batteries and apply this model to develop improved BPM materials with reduced neutralization overpotentials. Finally, we apply our findings to enhance energy recovery in the context of reversing electrolyte carbonation during CO_2 electrolysis. Our studies provide a mechanistic framework for understanding the current-voltage behavior of BPMs in mixed electrolytes and enable high-efficiency protonic to electrical energy conversion.

Results and Discussion

Mechanistic investigation of forward bias polarization in mixed electrolytes

In this work, two types of BPMs were employed: a homemade BPM, denoted by the nomenclature (Acid) | CEM | AEM | (Base), and the commercial Fumasep FBM, denoted by (Acid) | FBM | (Base) (see **Experimental Methods** for further detail). Unless the membranes are the subject of the experiment, FBM will be used, and these notations will be abbreviated to (Acid) | (Base) in the text. In addition, as all measurements of membrane voltage (V_{mem}) were made by sensing the electric potential of the acid solution with respect to the base solution, V_{mem} will be reported as a negative value, with polarization to less negative values indicating forward bias. Currents are reported based on measurements of electrical current through the external circuit, and hence positive currents correspond to forward bias polarization. In this study, to simplify the analysis of V_{mem} , we assume that the concentration of fixed charges in the CEM and AEM is 1 M, and that Donnan potentials at the membrane-electrolyte interfaces are constant at 0 mV. Hence, changes in V_{mem} reflect only changes in the bipolar junction voltage (V_j).³⁸ Here, we will use the term *weak electrolytes* to refer to charged bases whose conjugate acids have a $\text{p}K_{\text{a}} < 14$ (e.g., OAc^-) or charged acids with a $\text{p}K_{\text{a}} > 0$ (e.g., NH_4^+), and the term *strong electrolytes* to refer to H^+ and OH^- .

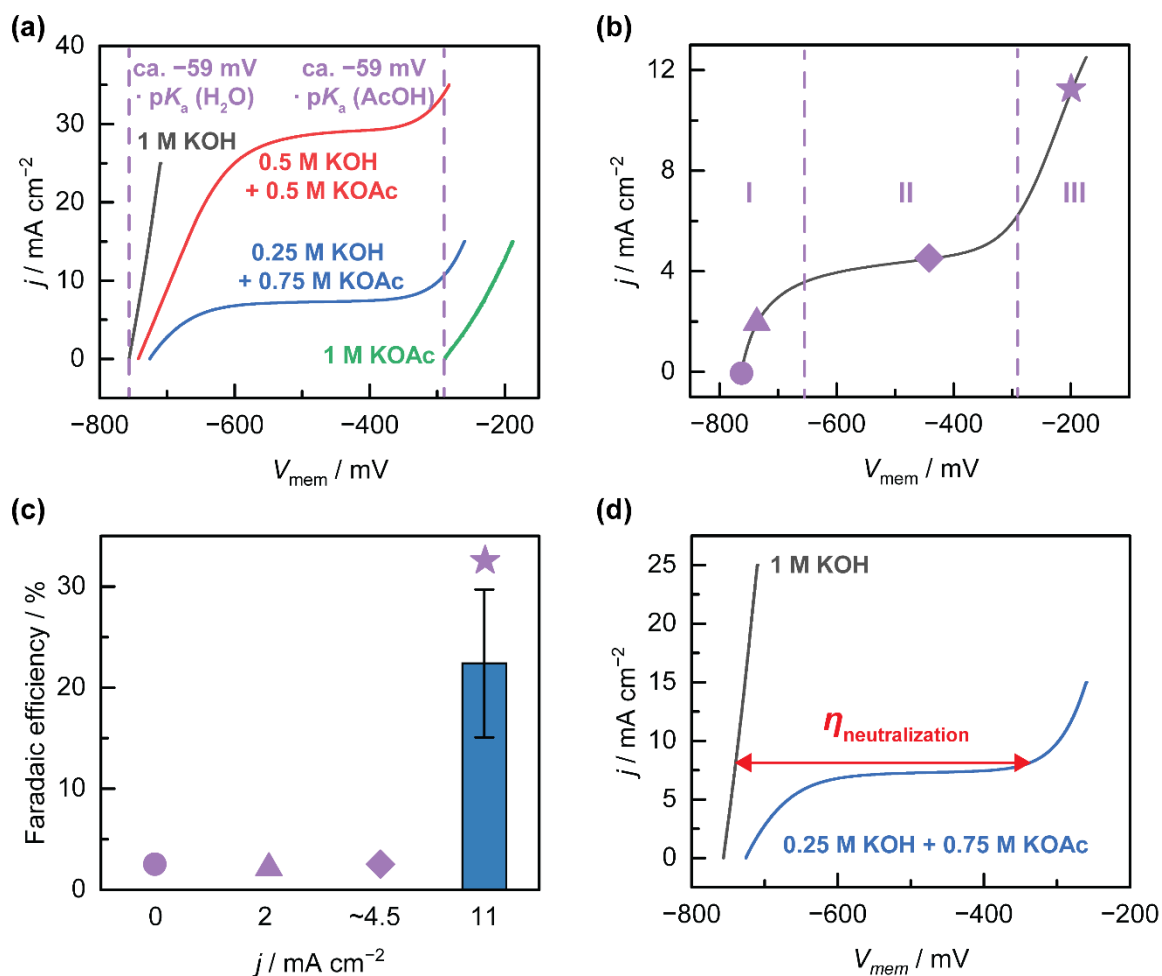


Figure 2. (a) Forward bias polarization curve of $1\text{ M H}_2\text{SO}_4 | \text{CEM} | \text{AEM} | x\text{ M KOH} + y\text{ M KOAc}$ (where $x + y = 1$). (b) Forward bias polarization curve of $1\text{ M H}_2\text{SO}_4 | \text{FBM} | 0.5\text{ M KOH} + 0.5\text{ M KOAc}$, with different regions delineated. (c) Faradaic efficiency for AcOH based on analysis of aliquots taken from acid compartment after controlled current or voltage polarization at points indicated in (b). The error bar in (c) represents the standard deviation of three independent replicates. (d) Forward bias polarization curve of $1\text{ M H}_2\text{SO}_4 | \text{CEM} | \text{AEM} | 1\text{ M KOH}$ and $1\text{ M H}_2\text{SO}_4 | \text{CEM} | \text{AEM} | 0.25\text{ M KOH} + 0.75\text{ M KOAc}$, with the neutralization overpotential, $\eta_{\text{neutralization}}$, marked for 8 mA cm^{-2} .

Forward bias polarization is gated by acid-base equilibria. In order to understand how mixed electrolytes influence forward bias polarization behavior, we investigated a BPM cell containing a mixture of a hydroxide and acetate in the catholyte paired with a sulfuric acid anolyte. Specifically, we employed cells of the type $1\text{ M H}_2\text{SO}_4 | x\text{ M KOH} + y\text{ M KOAc}$ ($x + y = 1$), where OAc = acetate. KOH and KOAc were chosen due to the large separation in the $\text{p}K_a$ values for their conjugate acids (14 vs 4.75), allowing us to sample behavior over a wide basicity range. The open-circuit V_{mem} values for catholytes containing 1 M KOH , $0.75\text{ M KOH} + 0.25\text{ M KOAc}$ and $0.25\text{ M KOH} + 0.75\text{ M KOAc}$ were found to be close to $-59\text{ mV} \cdot \Delta\text{pH}$ (where $\Delta\text{pH} = \text{pH}_{\text{catholyte}} - \text{pH}_{\text{anolyte}}$) or, equivalently, $-59\text{ mV} \cdot \text{p}K_a(\text{H}_2\text{O})$, whereas that for the catholyte containing 1 M KOAc was close to $-59\text{ mV} \cdot \text{p}K_a(\text{AcOH})$ (**Figure 2(a)**). The $\text{p}K_a$ -pinned open-circuit V_{mem} value, or $V_{\text{p}K_a}$, for the latter case is consistent with our findings in our previous study,³⁸ in which we showed that ionic short-circuiting processes led to buffering of

the bipolar interface by the acid-base couple present ($\text{H}_2\text{O}/\text{OH}^-$ and AcOH/OAc^- , respectively). In the case of $1 \text{ M H}_2\text{SO}_4 \mid 0.75 \text{ M KOH} + 0.25 \text{ M KOAc}$ and $1 \text{ M H}_2\text{SO}_4 \mid 0.25 \text{ M KOH} + 0.75 \text{ M KOAc}$, the presence of OH^- ensures a high pH in the region of the AEM close to the bipolar interface, resulting in the open-circuit V_{mem} being dominated by the H^+/OH^- recombination couple and pinned to ca. $-59 \text{ mV} \cdot \Delta\text{pH}$ despite the presence of OAc^- . These open-circuit membrane voltages reflect the expected pH gradients at the bipolar interface.

The forward bias polarization curves display a high degree of complexity when mixed electrolytes are used. For the $1 \text{ M H}_2\text{SO}_4 \mid 1 \text{ M KOH}$ and $1 \text{ M H}_2\text{SO}_4 \mid 1 \text{ M KOAc}$ cells, we observed a monotonic current rise (**Figure 2(a)**), which must correspond to the recombination reactions in **Equation 1** and **Equation 2**, respectively.



Indeed, surveying other cells of the type $1 \text{ M H}_2\text{SO}_4 \mid 1 \text{ M KA}$ containing the monoprotic base A^- revealed similar forward bias polarization curves with monotonic current rising from the respective open-circuit V_{mem} values set by the $\text{p}K_{\text{a}}$ of each HA (**Figure S3**). In contrast to these single-component catholytes, in the presence of a mixture of hydroxide and acetate, the current rise is interrupted by a broad limiting current plateau (**Figure 2(a)**, red and blue traces). As the KOH: KOAc concentration ratio increases from 0.25:0.75 to 0.5:0.5, the limiting current density increases from 7.3 mA cm^{-2} to 29 mA cm^{-2} . This potential-independent limiting current is observed despite the large undepleted pool of OH^- in the bulk electrolyte that could undergo protonation at the bipolar interface. In addition, the V_{mem} at which additional current flows beyond the limiting plateau was found to overlap with the open-circuit V_{mem} of $1 \text{ M H}_2\text{SO}_4 \mid 1 \text{ M KOAc}$, occurring at ca. $-59 \text{ mV} \cdot \text{p}K_{\text{a}}(\text{AcOH})$ (**Figure 2(a)**). When an analogous series of cells of the type $x \text{ M H}_2\text{SO}_4 + y \text{ M NH}_4\text{Cl} \mid 1 \text{ M KOH}$ ($x + y = 1$) were polarized in forward bias (**Figure S4**), we observed identical behavior to the $1 \text{ M H}_2\text{SO}_4 \mid x \text{ M KOH} + y \text{ M KOAc}$ cells. Additionally, consistent with previous experimental^{38,39} and computational³³ reports, we observe that the presence of polyprotic buffer species in the cell $1 \text{ M H}_2\text{SO}_4 \mid 1 \text{ M K}_x\text{H}_y\text{PO}_4$ ($x + y = 3$), gave multiple limiting current plateaus with inflection points coinciding with ca. $-59 \text{ mV} \cdot \text{p}K_{\text{a}}(\text{H}_3\text{PO}_4)$ (-130 mV), ca. $-59 \text{ mV} \cdot \text{p}K_{\text{a}}(\text{H}_2\text{PO}_4^-)$ (-430 mV) and ca. $-59 \text{ mV} \cdot \text{p}K_{\text{a}}(\text{HPO}_4^-)$ (-620 mV), respectively (**Figure S5**). Together, these data reveal that the sigmoidal current-voltage profile is universal to electrolyte mixtures with species of different acidities, regardless of whether those species arise from a common polyprotic acid (e.g., phosphates), or are structurally distinct (e.g., the OH^-/OAc^- and H^+/NH_4^+ mixtures).

The foregoing experiments show how electrolyte mixtures impact the current-voltage behavior, but do not shed light on which reaction (**Equation 1** or **Equation 2**) is occurring at each voltage. We postulated that net protonation of a given species can only occur at V_{mem} values more positive than its corresponding $V_{\text{p}K_{\text{a}}}$. In order to determine the identity of the species being protonated at the bipolar junction, we polarized the $1 \text{ M H}_2\text{SO}_4 \mid 0.5 \text{ M KOH} + 0.5 \text{ M KOAc}$ cell galvanostatically or potentiostatically within the three distinct regions of the polarization curve (**Figure 2(b)**); chronopotentiograms/chronoamperograms in **Figure S6 – Figure S10**), and analyzed aliquots taken from the acid compartment via ^1H NMR to determine the AcOH concentration. No AcOH was detected for polarizations in the underlimiting (I) and

limiting (II) regions of the polarization curve (**Figure 2(c)**). Only when the cell was polarized in the overlimiting (III) region, where $V_{\text{mem}} > V_{\text{pKa}(\text{AcOH})}$, did we observe an appreciable concentration of AcOH, corresponding to ca. 22% faradaic efficiency (FE) relative to the total ionic current (**Figure 2(c)**); see section below for quantitative analysis of observed FE). AcOH was also produced at appreciable FEs when the cell was polarized to higher currents (22, 33 mA cm^{-2}) in the overlimiting region (**Figure S11**). The observation that AcOH is produced in net only when $V_{\text{mem}} > V_{\text{pKa}(\text{AcOH})}$ suggests that V_{mem} is directly correlated to the interfacial pH gradient and speciation at the bipolar junction. Since the pH within the CEM, which contains the strong acid H^+ , is unlikely to change, this observation implies that the increase in V_{mem} from -760 mV to -280 mV is consistent with the near-interfacial region of the AEM decreasing in pH from ca. 13 to ca. 4.76. This in turn indicates an accumulation of OAc^- and depletion of OH^- near the bipolar interface. This correlation of V_{mem} to the interfacial acid-base chemistry is discussed further in **Supplementary Discussion 1**. Indeed, when open-circuit V_{mem} measurements of the $1 \text{ M H}_2\text{SO}_4 \mid x \text{ M KOH} + y \text{ M KOAc}$ cells were performed immediately after collection of the forward bias polarization curves, the open-circuit transients for return to the unpolarized equilibrium state were found to parallel the polarization curves, with inflection points conserved at the same $V_{\text{pKa}(\text{AcOH})}$ value (**Figure S14**). These observations highlight the strong correlation between the speciation at the bipolar interface, the interfacial pH differential, and V_{mem} .

Importantly, these results highlight that a substantial overpotential is imposed on the neutralization of a strong electrolyte (OH^-) by the presence of the weaker electrolyte (OAc^-). Despite the fact that OH^- protonation is exergonic at all voltages positive of the open-circuit value, the current plateaus in the presence of OAc^- , even in electrolyte mixtures where OAc^- is the minority species (**Figure 2(a)**). Consequently, accessing an OH^- neutralization current in excess of the limiting value requires the application of a substantial *neutralization overpotential*, $\eta_{\text{neutralization}}$, which subtracts from the thermodynamic potential available in the H^+/OH^- neutralization reaction. For example, at 8 mA cm^{-2} current density, even though OH^- is expected to carry all the neutralization current, V_{mem} for $1 \text{ M H}_2\text{SO}_4 \mid 1 \text{ M KOH}$ is -750 mV, but V_{mem} for $1 \text{ M H}_2\text{SO}_4 \mid 0.25 \text{ M KOH} + 0.75 \text{ M KOAc}$ is -340 mV, which translates into $\eta_{\text{neutralization}} = 410$ mV (**Figure 2(d)**). We note that this neutralization overpotential will increase as the concentration of the weak acid/base increases and for $\text{p}K_a/\text{p}K_b$ values further removed from that of the strong acid/base. Collectively, the foregoing findings evince that the net protonation of a given species A^- can only occur at $V_{\text{mem}} < V_{\text{pKa}(\text{HA})}$, and that the presence of a weak electrolyte can result in large overpotentials for the neutralization of a strong electrolyte.

Forward bias limiting currents arise from interfacial ionic blockades. In order to shed additional light on the factors controlling the limiting current and the neutralization overpotential, we conducted several experiments varying the electrolyte composition. First, for cells of the type $1 \text{ M H}_2\text{SO}_4 \mid x \text{ M KOH} + x \text{ M KOAc}$ ($x = 0.5$ or 0.75), we held the concentration ratio between KOH and KOAc constant at 1:1 but increased the absolute concentration of KOH/KOAc from 0.5 to 0.75 M, and found that j_{lim} remained unchanged at ca. 4.3 mA cm^{-2} (**Figure 3(a)**). This shows that j_{lim} is sensitive to the concentration ratio of mixed electrolytes but not to their absolute concentrations.

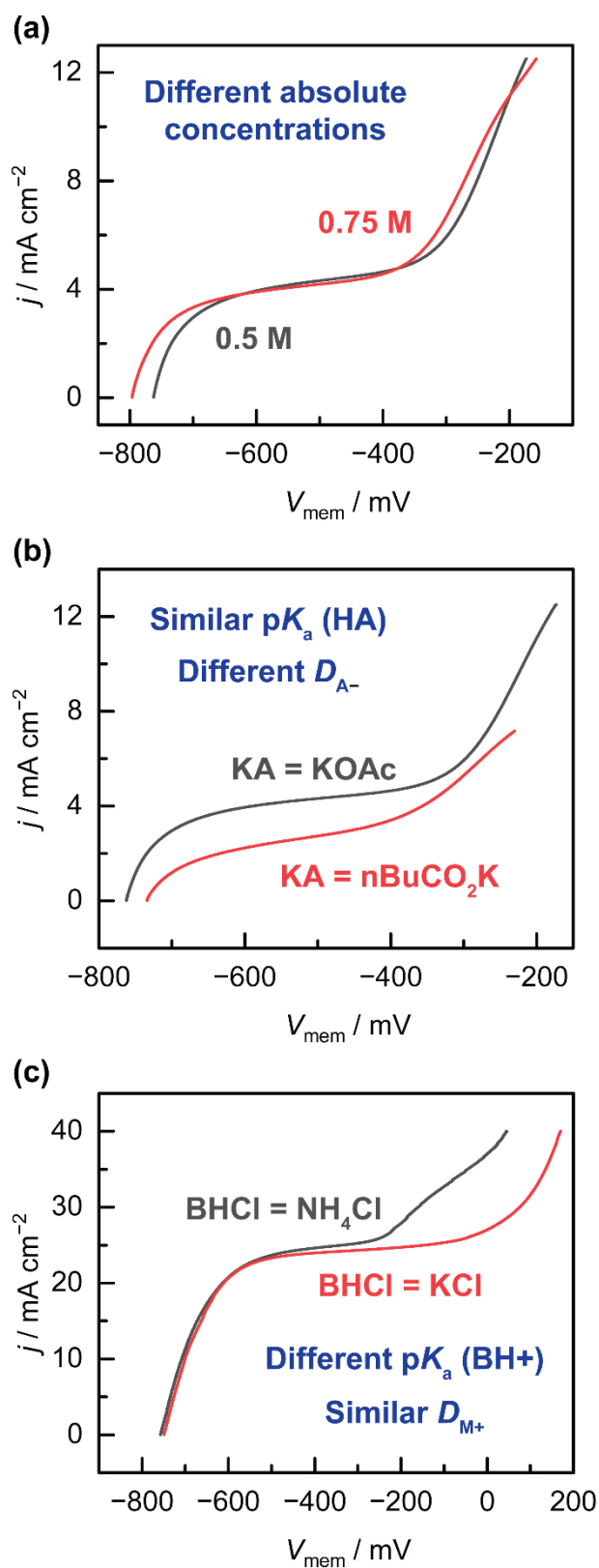


Figure 3. Forward bias polarization curves for (a) 1 M H_2SO_4 | FBM | x M KOH + x M KOAc ($x = 0.5$ or 0.75), (b) 1 M H_2SO_4 | FBM | 0.5 M KOH + 0.5 M KA ($A^- = \text{OAc}^-$ or nBuCO_2^-), and (c) 0.5 M H_2SO_4 + 0.5 M MCl | FBM | 1 M KOH ($M^+ = \text{NH}_4^+$ or K^+).

Next, we substituted acetate for n-butyrate in the analyte compartment. Specifically, for cells of the type 1 M H₂SO₄ | 0.5 M KOH + 0.5 M KA (A⁻ = OAc⁻ or nBuCO₂⁻, where nBuCO₂ = butyrate), acetate and butyrate have similar proton affinities (pK_a = 4.76 for AcOH, 4.82 for nBuCO₂H) but distinct diffusion coefficients ($D_{\text{OAc}^-} = 1.089$, $D_{\text{nBuCO}_2^-} = 0.868$).⁴⁰ This substitution leads to a lower j_{lim} for the nBuCO₂K cell (ca. 2.7 mA cm⁻²) than the KOAc cell (ca. 4.3 mA cm⁻²) (**Figure 3(b)**), correlated with $D_{\text{nBuCO}_2^-}$ being lower than D_{OAc^-} . We note that V_{mem} for the current onset in the overlimiting region is conserved between the two cells, owing to $V_{\text{pKa}(\text{AcOH})} \text{ ca. } V_{\text{pKa}(\text{nBuCO}_2\text{H})}$. Conversely, with cells of the type 0.5 M H₂SO₄ + 0.5 M MCl | 1 M KOH (M⁺ = NH₄⁺ or K⁺) (note that the electrolyte mixture is now in the acid instead of the base compartment), we selected unreactive ions with similar diffusion coefficients ($D_{\text{NH}_4^+} = D_{\text{K}^+} = 1.957$) but different proton affinities (pK_a = 9.25 for NH₄⁺, 14 for K⁺ (H₂O)). Here, j_{lim} was found to be almost identical in value between the two cells (ca. 24 mA cm⁻²) (**Figure 3(c)**). To determine whether j_{lim} depended on the diffusion coefficient of only the unreactive electrolyte or both the unreactive and reactive electrolyte, we examined the cell with 0.5 M NH₄Cl + 0.5 M KCl | 1 M KOH, and measured a j_{lim} that was significantly lower (ca. 7 mA cm⁻²) than that with the 0.5 M H₂SO₄ + 0.5 M KCl anolyte (24 mA cm⁻²) (**Figure S15**). These findings demonstrate that j_{lim} depends on the diffusion coefficients of both the unreactive and reactive electrolyte, but not on the acid-base thermochemistry of either electrolyte.

Collectively, the foregoing data depicting the effect of electrolyte composition on forward bias polarization suggest a transport model whereby different reactive species in the mixed electrolyte (e.g., OH⁻ vs OAc⁻) compete for a finite number of fixed charge sites to charge-pair with in the membrane (e.g., AEM). Specifically, we propose that site competition on the order of the depletion layer thickness (ca. 4 – 10 nm)^{33,41} controls speciation at the near-interfacial region (within several nm) of the bipolar junction and consequently the V_{mem} , and that site competition on diffusional lengthscales (ca. 10s – 100s of μm) controls speciation within the bulk of the AEM and consequently the value of j_{lim} . Our putative model reflects the following boundary conditions: (a) the composition within the AEM near the AEM | Base interface is controlled by the Donnan equilibria for OH⁻ and OAc⁻;³³ (b) OH⁻ and OAc⁻ are the only mobile charges within the AEM, and hence their concentrations must sum to the fixed charge concentration everywhere in the AEM except at the interfacial depletion region; (c) V_{mem} directly reports on the interfacial pH gradient, and hence reveals the speciation of OH⁻, OAc⁻ and AcOH at the bipolar interface.^{33,41} Applying these constraints, postulated concentration profiles as a function of the region of the polarization curve in the near-interfacial and bulk regions of the AEM for OH⁻, OAc⁻ and AcOH are depicted in **Figure 4(a)**, and postulated pH profiles across the BPM in the same regions are depicted in **Figure 4(b)**. These profiles are in qualitative agreement with a previous computational study.³³

At open-circuit, we postulate that the concentration ratio of OH⁻:OAc⁻ in the bulk of the AEM becomes identical to that in the base solution upon complete equilibration (**Figure S16**). The concentrations of OH⁻ and OAc⁻ near the interface, however, depend on neutralization equilibria attained between H⁺, OH⁻ and OAc⁻, which we envision to lead to a much lower OH⁻:OAc⁻ ratio than that in the bulk due to the higher reactivity of OH⁻ compared to OAc⁻ (**Figure S16**).

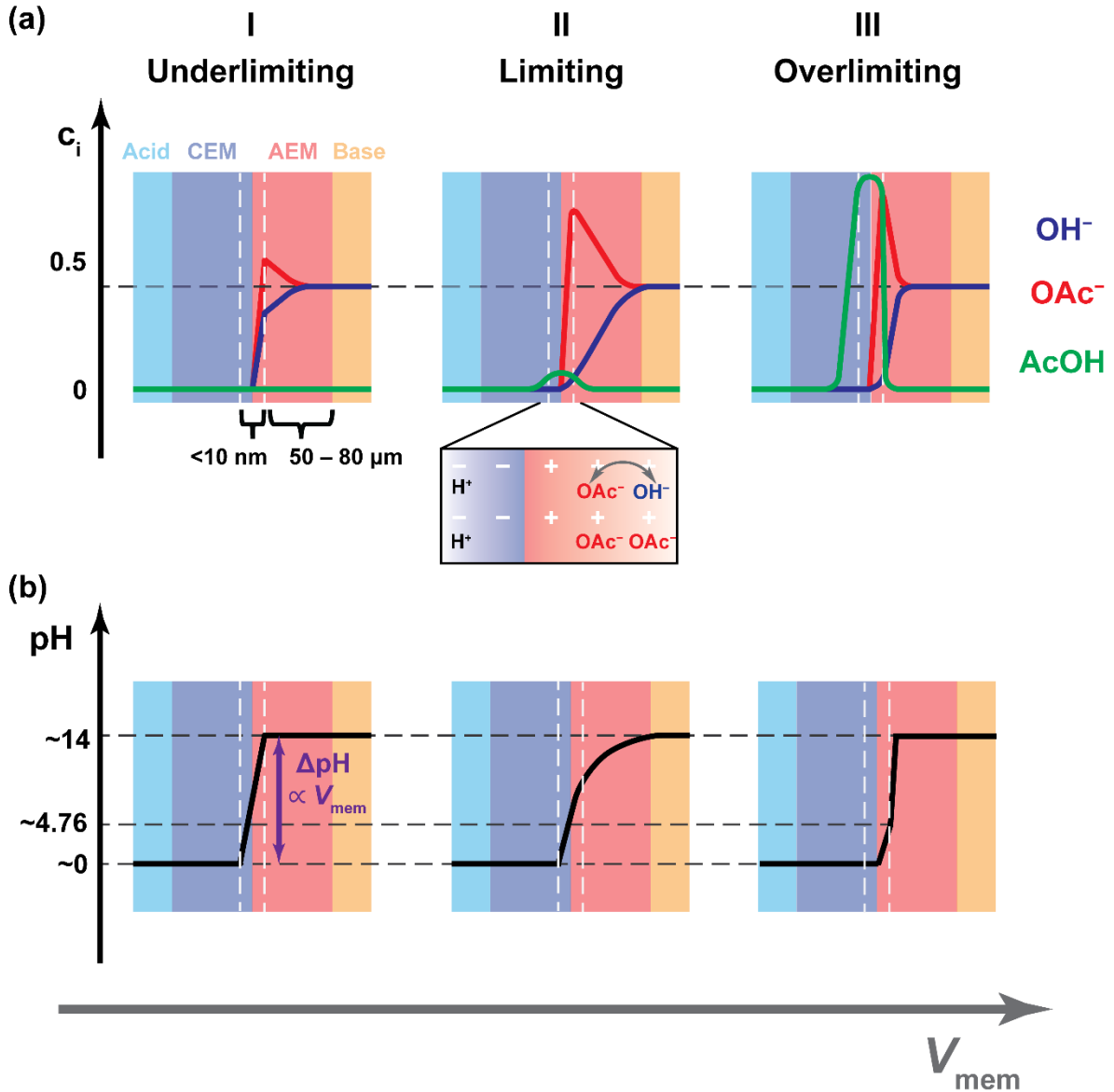


Figure 4. (a) Postulated concentration profiles of OH^- , OAc^- , and $AcOH$ in different regions of the polarization curve (as demarcated in **Figure 2(b)**). Vertical dashed lines indicate the near-interfacial regions, where equilibration of the proton activity with the electric potential profile in the bipolar interface is rapid. (b) pH profiles in different regions of the polarization curve. Profiles in (a) and (b) are qualitatively plotted based on the initial quasi-steady-state conditions attained upon short-duration polarization of the cell (whereby concentrations of OH^- and OAc^- in the solution have not significantly changed). The fixed charge concentration in the AEM is assumed to be 1 M to simplify the analysis.

As the cell is polarized into the underlimiting region (region I), the net protonation of OH^- according to **Equation 1** allows the passage of current at the bipolar interface, resulting in the steep current-voltage slope (**Figure 2(b)**, region I). Since $V_{pKa(H_2O)} < V_{mem} < V_{pKa(AcOH)}$, OH^- is the only base species capable of being protonated in net within this region. This results in the near-interfacial region of the AEM being gradually depleted in reactive OH^- and enriched in unreactive OAc^- with increasing V_{mem} (**Figure 4(a)**, region I). Since the applied field across the BPM induces the migration of both OH^- and OAc^- towards the bipolar interface, the

unreactive OAc^- accumulates in the bulk of the AEM while the reactive OH^- depletes (**Figure 4(a)**, region I).

Entering the limiting region (region II), the current flatlines and becomes roughly voltage-independent (**Figure 2(b)**, region II). Since $V_{pK_a(\text{H}_2\text{O})} < V_{\text{mem}} < V_{pK_a(\text{AcOH})}$, the majority of the current is still due to OH^- protonation, as the interfacial pH gradient does not yet permit significant net OAc^- protonation. We propose that current passed at the bipolar interface is now limited by OH^- diffusion. The near-interfacial region of the AEM is now almost completely depleted of the reactive OH^- and dominated by the unreactive OAc^- (**Figure 4(a)**, region II). Due to the rigidity of fixed charge groups within the AEM, the transport of OH^- to reach the interfacial region must be accompanied by coupled motion with OAc^- , the only other mobile species, in order to avoid electrical charge gradients and maintain electroneutrality. This results in a type of place-exchange mechanism for OH^- transport, whereby a OH^- ion diffusing towards the interface swaps sites with an OAc^- ion diffusing away from the interface (**Figure 4(a)**, region II, blowup), leading to the observed potential-independent polarization curve. The observation that j_{lim} depends on the $\text{OH}^-:\text{OAc}^-$ concentration ratio (**Figure 2(a)**) and the diffusion coefficient of both the reactive and unreactive species (**Figure 3(b) – (c)**, **Figure S15**) is evidence for this electrolyte exchange mechanism, and furthermore suggests that the overall process is rate-limited by the aggregate place exchange dynamics. This is a type of ion-ion correlated motion, which has been computationally demonstrated to play a significant role in ion exchange membranes.⁴² We term this phenomenon an *ionic blockade*, whereby an unreactive weak electrolyte inhibits the transport of a reactive strong electrolyte inside an ion exchange membrane. Consequently, the concentration of OH^- in the bulk of the AEM continues to decrease, whereas the concentration of OAc^- continues to increase as the V_{mem} is swept more positively. An alternative explanation for the limiting region is that net protonation current can only be passed when the AcOH at the bipolar interface diffuses into the AEM and reacts with OH^- , but this is a less plausible mechanism (see **Supplementary Discussion 2**). Finally, to rule out the co-ion playing a significant role in controlling j_{lim} , we polarized the cells $1 \text{ M H}_2\text{SO}_4 \mid 0.625 \text{ M MOH} + 0.375 \text{ M MOAc}$ ($\text{M}^+ = \text{Li}^+, \text{Na}^+ \text{ or } \text{K}^+$) and found a minor dependence on the identity of the co-ion (**Figure S18**). Together, the evidence suggests that this ionic blockade phenomenon imposed by unreactive weak acids/bases in the CEM/AEM is the origin of the aforementioned neutralization overpotential.

Finally, as the cell is polarized past $V_{pK_a(\text{AcOH})}$, the current rapidly takes off again (**Figure 2(b)**, region III). This is due to the net protonation of OAc^- being turned on, which clears the ionic blockade and allows for unfettered flow of both OH^- and OAc^- . The concentration of OH^- rises in the bulk of the AEM and the concentration of OAc^- decreases as the concentration polarization from the ionic blockade is reduced. In this region, the current is expected to partition between OH^- protonation and OAc^- protonation as per their relative migration fluxes through the AEM (**Equation 3**, derivation in **Supplementary Discussion 3**).

$$\frac{N_{\text{OH}^-}}{N_{\text{OAc}^-}} = \frac{D_{\text{OH}^-} c_{\text{OH}^-}}{D_{\text{OAc}^-} c_{\text{OAc}^-}}$$

Equation 3

This explains the 22% FE for AcOH production (**Figure 2(c)**), which results from $D_{\text{OAc}^-}: D_{\text{OH}^-} = 1:4$ when the solution $\text{OH}^-:\text{OAc}^-$ concentration ratio is kept at 1:1. Further evidence corroborating our model of site competition comes from the open-circuit equilibration data, where we find that relative diffusive fluxes of OH^- and OAc^- control the near-interfacial composition of the AEM and the resulting V_{mem} (**Supplementary Discussion 4**). We note that some of the AcOH present in the AEM can be neutralized by OH^- , leading to an asymmetric concentration profile favoring AcOH diffusion into the AEM that leads to a disparity between the FE measured with our methodology (see **Supplementary Information**) compared to that predicted by **Equation 3**. Indeed, we see FEs decreasing to below ca. 20% at higher current densities (**Figure S11; Figure S21**), but postulate that this asymmetry in acetic acid diffusion is a minor contributor at modest current densities (**Figure 2(c)**). Collectively, our studies on electrolyte variation have established a mechanistic basis for the forward bias current-voltage behavior of BPMs containing mixed electrolytes of different acidities/basicities.

Implications of the mechanistic model for forward bias BPM galvanic cells

The preceding mechanistic picture is relevant to a number of BPM galvanic cell types including H_2 fuel cells^{43,44} and aqueous redox flow batteries.^{29,30} For example, BPMs can be employed in fuel cells to pair facile hydrogen oxidation kinetics in acid with the use of earth-abundant catalysts for oxygen reduction in base.⁴³ The production of water at the bipolar junction in forward bias also endows fuel cells with the property of self-humidification.⁴³ However, the operation of fuel cells can be complicated by the formation and accumulation of (bi)carbonates in the alkaline electrolyte due to exposure to ambient CO_2 .³⁶

To understand the effect of trace carbonate on the performance of a $\text{H}_2\text{SO}_4 \mid \text{KOH}$ BPM fuel cell, we measured polarization curves of cells of the type $1 \text{ M } \text{H}_2\text{SO}_4 \mid \text{FBM} \mid x \text{ M } \text{KOH} + y \text{ M } \text{K}_2\text{CO}_3$ ($x + 2y = 1$) (**Figure 5(a)**). We find that even with pristine KOH solutions, a limiting current region develops, due to the presence of trace carbonate from CO_2 absorption. Importantly, the limiting current decreases dramatically from ca. 45 to ca. 14 mA cm^{-2} as the concentration of K_2CO_3 present increases from trace levels to 0.125 M. Following from the model developed above, this limiting current results from the accumulation of CO_3^{2-} and HCO_3^- species at the BPM junction, inhibiting OH^- transport to the interface. In this case, it is expected that only OH^- and CO_3^{2-} are protonated at currents below the limiting current, and that HCO_3^- is only protonated at currents above the limiting current. Operating the BPM at a V_{mem} that results in bicarbonate protonation and CO_2 formation is an option, but the resulting ca. 450 mV neutralization overpotential will sap the power output of the fuel cell, particularly given that the peak power point of most hydrogen fuel cells occurs in the high-current range at $V_{\text{mem}} > -200$ mV. Importantly, ionic blockading by (bi)carbonates occurs even when these species are minority constituents of the strongly alkaline electrolyte and the bulk of the current is carried by OH^- ions (**Figure 5(b)**). In addition, gas evolution at the bipolar junction can lead to delamination, which can be problematic for conventional bipolar membranes (see below for a detailed discussion of this topic). We note that if the basic solution progressively accumulates (bi)carbonate, operating in the under-limiting and limiting regions will not clear these species from the cell, and so periodic polarization in the over-limiting region may be necessary to re-establish the hydroxide pool. Notwithstanding, our model explains the pernicious effect of even trace (bi)carbonates on the efficiency of forward bias BPM fuel cells. This motivates the development of strategies for raising the limiting current (see below) to enable access to high

power densities for fuel cells as well as other galvanic devices, such as redox flow batteries (see **Supplementary Discussion 5**).

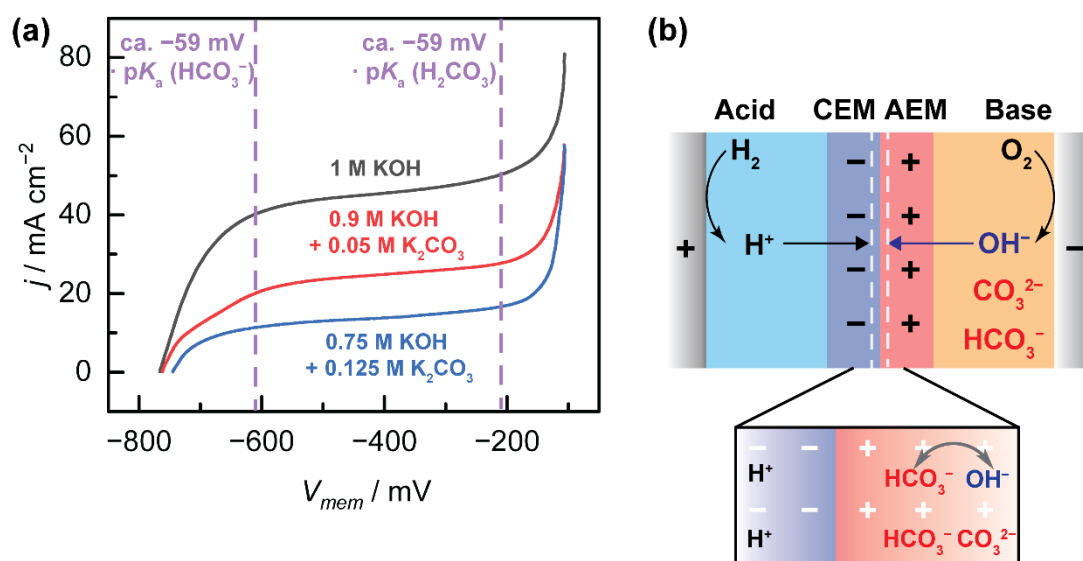


Figure 5. (a) Forward bias polarization curves for the cells $1 \text{ M H}_2\text{SO}_4 \mid \text{FBM} \mid x \text{ M KOH} + y \text{ M K}_2\text{CO}_3$ ($x + 2y = 1$). Note that the current takeoff in the high current region is pinned to the pK_a of 3.49 for H_2CO_3 . (b) Cell schematic showing the faradaic reactions at the electrodes and the ionic reactions within the BPM for a forward bias BPM H_2 fuel cell. CO_3^{2-} and HCO_3^- ions formed from CO_2 absorption into the alkaline electrolyte accumulate in the AEM and impose an ionic blockade on OH^- transport.

Materials design enables enhancement of limiting current for forward bias BPM galvanic cells

Analysis of forward bias BPM galvanic cells using our mechanistic framework revealed the importance of high limiting currents, and motivated us to explore the experimental handles that were available to control the limiting current. We first investigated the effect of varying the properties of the membrane. Using cells of the type $0.5 \text{ M NH}_4\text{Cl} + 0.5 \text{ M H}_2\text{SO}_4 \mid \text{CEM} \mid \text{FAA-3-50} \mid 1 \text{ M KOH}$, where the CEM was varied in thickness, we observed that j_{lim} (considered at $V_{\text{mem}} = -450 \text{ mV}$) decreased from 44 mA cm^{-2} to 26.6 mA cm^{-2} as the CEM thickness increased from $9 \mu\text{m}$ to $124 \mu\text{m}$ (**Figure 6(a)**). However, as the CEM thickness increased past the threshold value of $124 \mu\text{m}$ to $178 \mu\text{m}$ and subsequently $254 \mu\text{m}$, j_{lim} remained invariant at ca. 12.5 mA cm^{-2} (**Figure 6(a)**). We suggest that this non-monotonic change in j_{lim} can be attributed to the relative lengthscale of the thickness of the CEM (m) relative to the thickness of the diffusional boundary layer (δ) for the electrolyte exchange mechanism described in the preceding section (albeit applied to H^+/NH_4^+ exchange here) (**Figure 6(b)**). Although we previously established that the overall electrolyte exchange rate depends on both the reactive and unreactive ion, for simplicity, only the concentration profile for NH_4^+ has been depicted here. We note that the concentration profiles for NH_4^+ and H^+ should be inversely correlated, since no other counterions for the AEM exist. When $m > \delta$, then the diffusional boundary layer is entirely contained within the CEM and varying m has no bearing on the rate

of NH_4^+/H^+ exchange (**Figure 6(b)**). Conversely, when $m < \delta$, then variations in m result in changes in the rate of NH_4^+/H^+ rate. This is due to the effective diffusion coefficient of NH_4^+ being lower in the CEM than in solution, i.e. $D_{\text{NH}_4^+ (\text{CEM})} < D_{\text{NH}_4^+ (\text{Solution})}$. Consequently, the rate of NH_4^+ diffusion exchange is slower within the CEM than in solution. In addition, the ionic blockade effect of NH_4^+ on H^+ transport only occurs within the CEM, where there are no mobile anions and ion-ion correlations occur. Hence, the smaller the value of m , the faster the net NH_4^+/H^+ exchange, and the higher the value of j_{lim} (**Figure 6(b)**). This analysis brackets δ between 50 and 124 μm for the experiments in **Figure 6(a)**. These membrane thickness variation data demonstrate a materials handle for tuning j_{lim} and further support the notion that sluggish diffusion impeded by ionic place-exchange in the membrane is the origin of the limiting current.

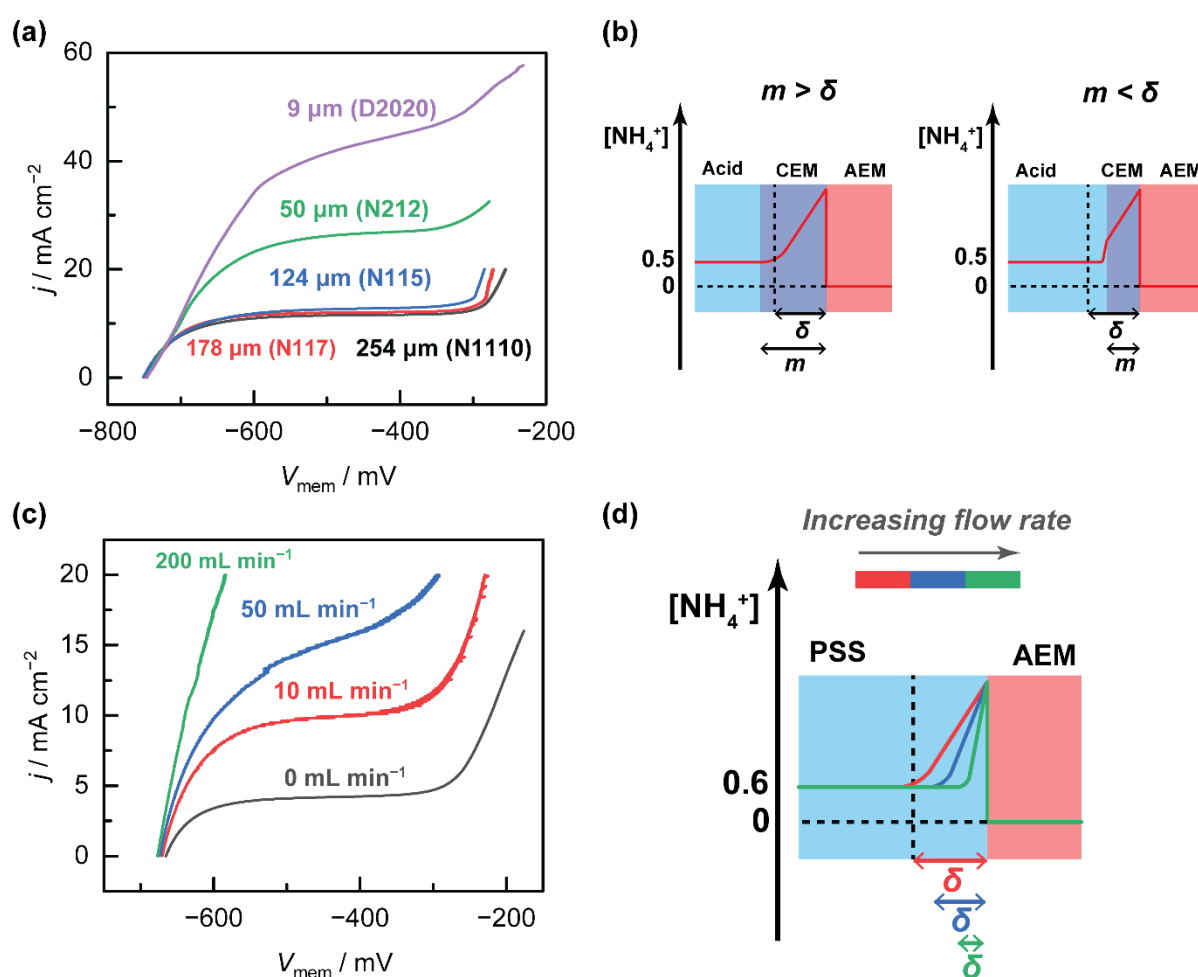


Figure 6. (a) Forward bias polarization curve of 0.5 M H_2SO_4 + 0.5 M NH_4Cl | CEM | AEM | 1 M KOH, wherein CEM thickness = 9, 50, 124, 178 or 254 μm (see **Table S2** for list of CEMs used). (b) Putative concentration profiles for NH_4^+ in the CEM and acid solution when CEM thickness (m) is larger or smaller than the diffusional boundary layer thickness (δ). (c) Forward bias polarization curve of 0.4 M PSS-H + 0.6 M PSS- NH_4 | AEM | 1 M KOH with varying flow rates. (d) Concentration profile for NH_4^+ in the PSS solution as a function of flow rate.

Finally, with mounting evidence that the limiting region is diffusively controlled, we sought to design a BPM system that afforded dynamic control over the current-voltage characteristics of the limiting region. In electrochemical systems, improved transport of species to a reactive surface of an electrode can be induced by introducing advection (e.g., by stirring the solution or the use of a rotating electrode setup).⁴⁵ In order to set up a system where advection could be directly applied to the bipolar interface, we employed a hybrid liquid-membrane system with the cell 0.4 M PSS-H + 0.6 M PSS-NH₄ | AEM | 1 M KOH, where the CEM and the H⁺- and NH₄⁺-containing acid solution of a conventional BPM setup are replaced with a poly(4-styrene sulfonate) (PSS⁻) solution. Owing to its high molecular weight (M_w ca. 70 kDa on average), the PSS⁻ co-ion is size-excluded from crossing the AEM, and is able to form a stable bipolar interface, with the PSS-H solution playing the dual role of CEM and acid solution.³⁸ With this cell type, we were able to collect polarization curves with different flow rates applied to the bipolar interface. Indeed, as the flow rate increased from 0 to 200 mL min⁻¹, the current density considered at the same V_{mem} of -600 mV increased nearly fivefold from 3.4 mA cm⁻² to 17.4 mA cm⁻² (**Figure 6(c)**). This correlation can be explained by the thickness of the diffusional boundary layer shrinking with increasing flow rate, leading to steeper concentration gradients for NH₄⁺ and faster H⁺/NH₄⁺ exchange rates (**Figure 6(d)**). The polyelectrolyte advection data here are in agreement with the limiting region being diffusion-controlled, and demonstrate a facile methodology for controlling the value of j_{lim} in this region.

Together, the strategies introduced above provide additional levers for managing electrolyte speciation across the BPM, mitigation the effect of ionic blockades, and decreasing overpotential losses in BPM electrochemical devices.

Implications for forward bias BPM CO₂ electrolyzers

The electrocatalytic CO₂ reduction reaction (CO₂RR) enables the production of carbon-based feedstocks and fuels powered by renewable electrical energy sources, and is a keystone transformation underpinning the clean energy transition.⁴⁶⁻⁴⁸ Selective CO₂ reduction requires an alkaline environment at the cathode interface.⁴⁹⁻⁵³ However, the absorption of CO₂ into alkaline solutions is a thermodynamically favorable process and leads to the formation of (bi)carbonates over time, lowering the energy efficiency for electrolysis.^{54,55} To circumvent this issue, CO₂ electrolyzers operating with acidic electrolytes (**Figure 7(a)**), which avoid carbonate formation, have been developed.⁵⁶⁻⁶¹ However, these systems universally rely on the presence of alkali metal cations in the electrolyte to engineer an alkaline pH swing local to the cathode surface.^{54,56} This leads to the development of a large pH gradient between the alkaline cathode surface and the bulk acidic electrolyte, which can add a significant but oft-overlooked concentration overpotential to the overall cell voltage. Therefore, while attractive for avoiding carbonate formation and allowing improved CO₂ utilization, the operation of acidic CO₂ electrolyzers invariably incurs large energy losses in the form of large pH swing overpotentials.

Forward bias BPM systems comprising a basic catholyte and an acidic anolyte have been employed in CO₂ electrolyzers to enable regeneration of CO₂ from carbonated electrolytes in operando and increase overall CO₂ utilization (**Figure 7(b)**).⁶²⁻⁶⁵ However, owing to the limited understanding of the mechanism of forward-bias BPM operation in carbonate electrolytes, the utilization of this device construct for energy recovery has been largely ignored.⁶²⁻⁶⁴ In contrast to acidic CO₂ electrolyzers that operate with a locally alkaline pH swing, the incorporation of a BPM between the acid and base compartments theoretically engenders the ability to transduce the chemical potential gradient into an electrical potential

gradient that can offset part of the cell voltage (**Figure 7(c)**). Hence, forward bias BPM CO₂ electrolyzers represent an attractive and potentially more energy-efficient alternative to acidic CO₂ electrolyzers. However, the lack of understanding of forward bias operation with carbonate electrolytes impedes the development of strategies to further improve the efficiency of CO₂ electrolyzers via BPM incorporation.

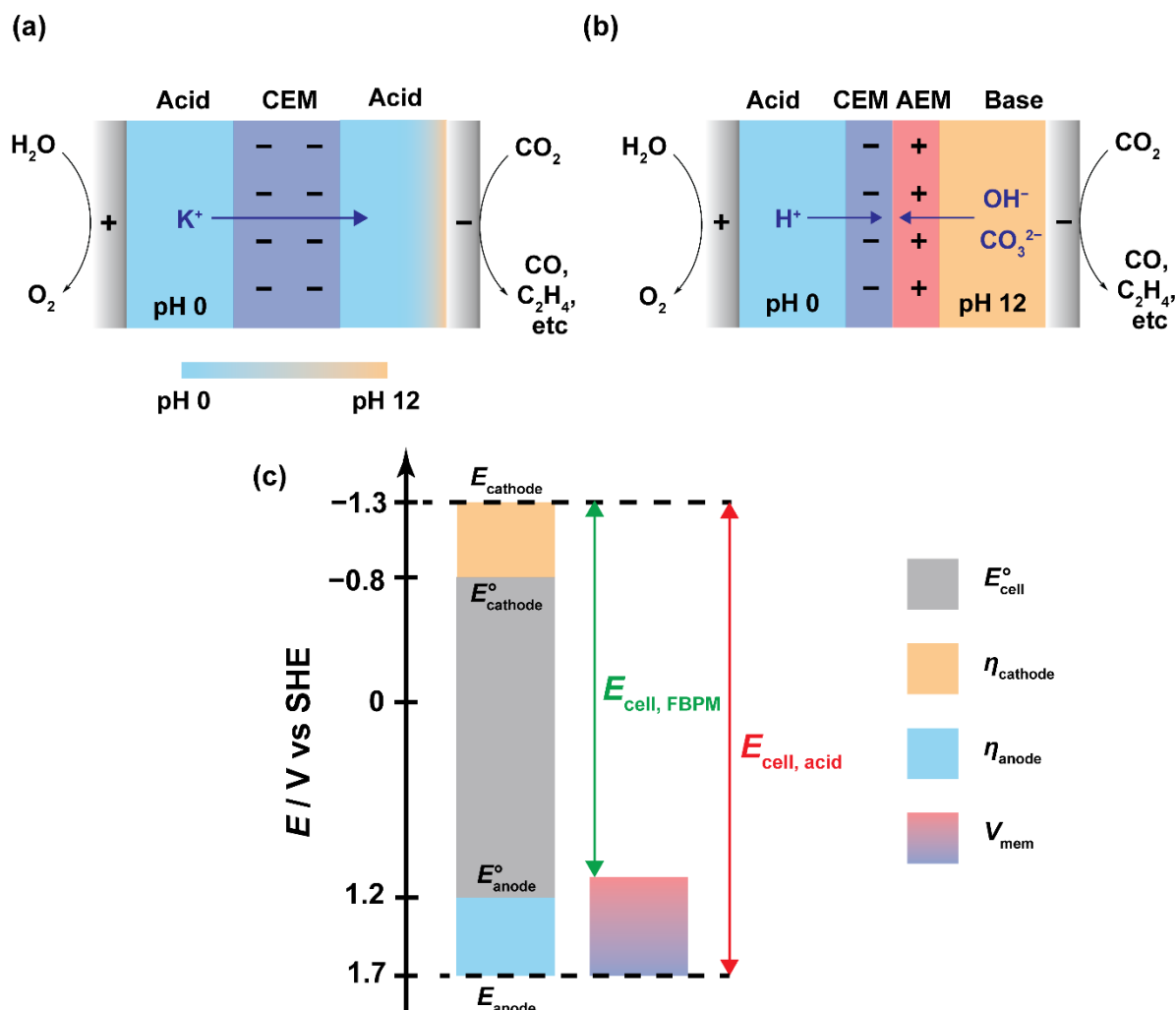


Figure 7. Cell schematics for (a) an acidic CO₂ electrolyzer employing an interfacial pH swing and (b) a forward bias BPM CO₂ electrolyzer. (c) Corresponding cell voltage breakdowns for (a) and (b), showing the voltage offset enabled by the BPM. E_{anode}° and $E_{\text{cathode}}^{\circ}$ refer to thermodynamic cell potentials in pH 0 and 12, respectively. Ohmic losses are assumed to be identical between the two types of cells and are not treated in this analysis. Approximate values are taken from the literature.^{54,56}

In order to understand the intrinsic forward bias polarization behavior of a BPM cell containing (bi)carbonates, we collected polarization curves for 1 M H₂SO₄ | 1 M K_xH_yCO₃ (x + y = 2). Analogous to the 1 M H₂SO₄ | x M KOH + y M KOAc mixed electrolyte cells, the open-circuit V_{mem} values for the K₂CO₃ cell and the KHCO₃ cell were found to pin to ca. -59 mV·pK_a (HCO₃⁻) and ca. -59 mV·pK_a (H₂CO₃) (**Figure 8(a)**). In addition, we observed polarization behavior for both cells that was analogous with the 1 M H₂SO₄ | x M KOH + y M

KOAc cells: the KHCO_3 cell showed current takeoff from the open-circuit voltage (**Figure 8(a)**) similar to the $1\text{ M H}_2\text{SO}_4 \mid 1\text{ M KOAc}$ cell (**Figure 2(a)**), whereas the K_2CO_3 cell exhibited a plateau current between V_{mem} values pinned to ca. $-59\text{ mV} \cdot \text{p}K_{\text{a}}(\text{HCO}_3^-)$ and ca. $-59\text{ mV} \cdot \text{p}K_{\text{a}}(\text{H}_2\text{CO}_3)$ (**Figure 8(a)**), analogous to the $1\text{ M H}_2\text{SO}_4 \mid x\text{ M KOH} + y\text{ M KOAc}$ ($x = 0.5, y = 0.5$ or $x = 0.75, y = 0.25$) cells (**Figure 2(a)**). Applying the foregoing mechanistic model, we expect that only CO_3^{2-} will be protonated in net in the underlimiting and limiting regions, and that net HCO_3^- protonation and CO_2 evolution can only occur at $V_{\text{mem}} > V_{\text{p}K_{\text{a}}(\text{H}_2\text{CO}_3)} = \text{ca. } -380\text{ mV}$ (**Figure 8(a)**). Operating at membrane voltages lower than this value will lead to progressive accumulation of the bicarbonate in the catholyte (**Figure 8(b)**) and thus operation at membrane voltages greater than this value is essential for continuous CO_2 clearance and steady state operation (**Figure 8(c)**). Consequently, the maximum electrical work recoverable is -380 mV rather than the -710 mV corresponding to the full 0-12 pH differential across a typical CO_2 electrolyzer.^{56,61} Nonetheless, this recovered voltage is a substantial fraction (54%), of that required to sustain the pH gradient, which is otherwise lost to heat in acidic pH swing CO_2 electrolyzers (**Figure 7(a)**). These findings establish a quantitative basis for the expected V_{mem} for a forward bias BPM regenerating CO_2 , and highlight the leveling effect that the $\text{p}K_{\text{a}}$ of H_2CO_3 can have on the resultant V_{mem} .

High-current forward bias BPM operation requires efficient CO_2 removal. In contrast to the $1\text{ M H}_2\text{SO}_4 \mid x\text{ M KOH} + y\text{ M KOAc}$ cells, we observe a second plateau for the $1\text{ M H}_2\text{SO}_4 \mid 1\text{ M K}_x\text{H}_y\text{CO}_3$ cells at higher current densities that was absent for the former. We postulate that the current density of the second plateau in **Figure 8(a)** corresponds to the diffusion-limited rate of CO_2 removal from the bipolar junction. Specifically, we posit that the low solubility of CO_2 in aqueous acidic media and the low gas permeability of the BPM results in the trapping of CO_2 bubbles, which saturate the bipolar interface with dissolved CO_2 . The elevated local CO_2 could in turn back-equilibrate with H_2O to produce H^+ and HCO_3^- which buffer against the further injection of charge carriers from the CEM and AEM into the bipolar junction. The above model predicts that this issue could be overcome with a bipolar interfacial structure that allowed for rapid CO_2 clearance. To test this hypothesis, we replaced the H_2SO_4 solution and CEM with PSS-H solution. The resulting polarization curve of the $1\text{ M PSS-H} \mid 1\text{ M KHCO}_3$ cell exhibited only a monotonic rise in the over-limiting region without the current plateau, consistent with facile CO_2 gas bubble release from the non-trapping liquid-membrane interface formed between PSS-H and the AEM (**Figure 8(d)**). Alternative approaches that avoid the trapping of CO_2 (e.g., a porous⁶⁴ or microchanneled⁶³ CEM structure) have also been found to result in improved device performance, but these studies expose, for the first time, the mechanistic importance of CO_2 removal for enhancing V_{mem} . Taken together, these observations suggest that polarization of a (bi)carbonate-containing BPM cell in the over-limiting region can be limited by the rate of removal of the accumulated CO_2 , and that a hybrid liquid-membrane interface strategy can circumvent this issue by allowing rapid CO_2 clearance.

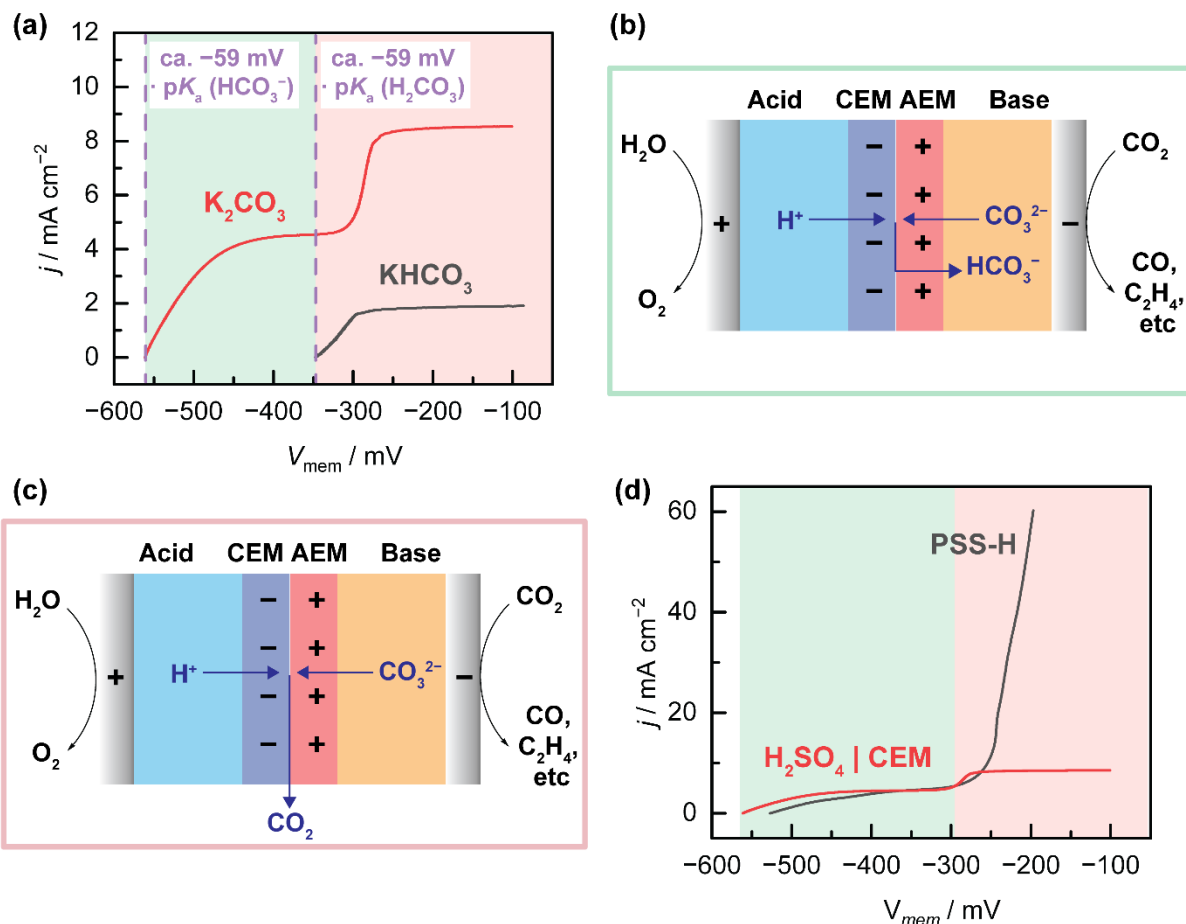


Figure 8. (a) Forward bias polarization curve of 1 M H_2SO_4 | CEM | AEM | 1 M $\text{K}_x\text{H}_y\text{CO}_3$ (where $x + y = 2$). Current-voltage regions where HCO_3^- is produced are shaded in green, and regions where CO_2 is produced are shaded in red. Cell schematics and polarization curves for a forward bias BPM CO_2 electrolyzer with a fully carbonated catholyte (e.g., 1 M K_2CO_3) operating in (b) the under-limiting and limiting regions (corresponding to the green regions) and (c) the over-limiting region (corresponding to the red regions). (d) Forward bias polarization curve of 1 M PSS-H | AEM | 1 M K_2CO_3 and 1 M H_2SO_4 | CEM | AEM | 1 M K_2CO_3 .

Revisiting BPM CO_2 electrolyzers where the forward bias mode is implemented to allow the recovery of liquid products from the CO_2RR ,^{66,67} a similar analysis can be performed for the impact of the region of operation on the speciation at the bipolar interface (**Figure S23**). Using a CO_2 electrolyzer that produces acetate in an alkaline catholyte as an example, our earlier findings (**Figure 2(c)**) reveal that acetate is only protonated at $V_{\text{mem}} > V_{\text{pKa}(\text{AcOH})}$ in the overlimiting region, and not in the underlimiting or limiting regions. This implication highlights two distinct modes of operation that are possible for such a device: (a) operating in the overlimiting region and continuously generating protonated liquid CO_2RR products at the bipolar interface, or (b) operating in the underlimiting and limiting regions and preferentially protonating hydroxide so as to concentrate acetate in the catholyte to enable more energy-efficient downstream separations outside the device. Operating in the concentrator mode would enable the recovery of a large V_{mem} from the pH gradient to offset the cell voltage, but would

require strategies for raising j_{lim} to match the currents passed at the electrodes, which can be accomplished via the use of a thin AEM layer or a flowing cationic polyelectrolyte (in place of the AEM) as discussed above. Hence, our studies illustrate how the current-voltage profile of the forward bias BPM platform can be a powerful atlas for manipulating ion speciation at the bipolar interface and controlling catholyte composition in a CO₂ electrolyzer.

Conclusions

Herein, by systematically varying the properties of electrolyte mixtures and membranes, we establish a general mechanistic framework for understanding the forward bias current-voltage profile of weak electrolyte-containing BPM cells. We find that the net protonation of a given acid/base onsets at voltages beyond those pinned by their $\text{p}K_{\text{a}}$ values. Furthermore, we reveal that an ionic blockade exerted by unreactive counterions can lead to limiting currents in forward bias. We expose the factors controlling this limiting current as well as materials design strategies for augmenting its magnitude, paving the way for designing galvanic cells that incorporate forward bias BPMs. Finally, we perform a detailed analysis on the implications of our studies to CO₂ electrolyzers, revealing how forward bias BPM electrolyzers can operate at lower cell voltages and higher efficiencies than acidic electrolyzers, as well as how knowledge of the current-voltage profile enables versatility in controlling ion speciation at the bipolar interface for performing liquid CO₂RR product recovery.

The results here shine a spotlight on the non-linear current-voltage relationship of forward bias BPMs interfaced with electrolyte mixtures, and the large, oft-overlooked overpotentials that can arise at the bipolar junction. Particularly pernicious is the levelling effect that weak acids/bases (e.g., HCO₃⁻) in the electrolyte can have on V_{mem} when they accumulate in the bipolar membrane and inhibit the transport of stronger acids and bases (e.g., OH⁻, CO₃²⁻), leading to large neutralization overpotentials. Ultimately, this ionic blockade effect stems from ion-exchange membranes being highly charge-selective but not chemoselective. We suggest that the development of membranes highly chemoselective for the transport of strong electrolytes could mitigate ionic blockade inhibition.⁶⁸ Together, the conclusions presented here provide a basis for predicting and understanding the forward bias polarization of BPMs with a multiplicity of mobile ions, and pave the way for the rational design of next-generation forward bias BPM applications.

Acknowledgements

We thank Shane Ardo and Shannon Boettcher for helpful discussions, and the entire Surendranath Lab for support. This work was supported by the Department of Energy under award number DE-SC0021634. This work made use of the MRSEC Shared Experimental Facilities at MIT, supported by the National Science Foundation under award number DMR-1419807. W.L.T. is supported by a National Science Scholarship awarded by the Agency for Science, Technology and Research (A*STAR), Singapore. H.D. is supported by Undergraduate Research Opportunities Program (UROP) awards from the MIT UROP office and the MIT Energy Initiative.

Author Contributions

W.L.T., H.D. and Y.S. conceptualized the project. W.L.T., H.D., A.C., and E.S. conducted experiments. W.L.T., H.D. and Y.S. wrote and edited the manuscript.

Declaration of Interests

The authors declare no competing interest.

References

- (1) Gileadi, E. *Physical Electrochemistry: Fundamentals, Techniques and Applications*; Wiley-VCH: Weinheim, 2011.
- (2) Tributsch, H.; Pohlmann, L. Electron Transfer: Classical Approaches and New Frontiers. *Science*. **1998**, *279* (5358), 1891–1895. <https://doi.org/10.1126/science.279.5358.1891>.
- (3) Kontturi, K.; Murtoimäki, L.; Manzanares, J. A. *Ionic Transport Processes*; Oxford University Press, 2008; Vol. 9780199533. <https://doi.org/10.1093/acprof:oso/9780199533817.001.0001>.
- (4) Pärnamäe, R.; Mareev, S.; Nikonenko, V.; Melnikov, S.; Sheldeshov, N.; Zabolotskii, V.; Hamelers, H. V. M.; Tedesco, M. Bipolar Membranes: A Review on Principles, Latest Developments, and Applications. *J. Memb. Sci.* **2021**, *617*, 118538. <https://doi.org/10.1016/j.memsci.2020.118538>.
- (5) Giesbrecht, P. K.; Freund, M. S. Recent Advances in Bipolar Membrane Design and Applications. *Chem. Mater.* **2020**, *32* (19), 8060–8090. <https://doi.org/10.1021/acs.chemmater.0c02829>.
- (6) Blommaert, M. A.; Aili, D.; Tufa, R. A.; Li, Q.; Smith, W. A.; Vermaas, D. A. Insights and Challenges for Applying Bipolar Membranes in Advanced Electrochemical Energy Systems. *ACS Energy Lett.* **2021**, *6*, 2539–2548. <https://doi.org/10.1021/acsenergylett.1c00618>.
- (7) Tufa, R. A.; Blommaert, M. A.; Chanda, D.; Li, Q.; Vermaas, D. A.; Aili, D. Bipolar Membrane and Interface Materials for Electrochemical Energy Systems. *ACS Appl. Energy Mater.* **2021**, *4* (8), 7419–7439. <https://doi.org/10.1021/acsaem.1c01140>.
- (8) Yan, Z.; Mallouk, T. E. Bipolar Membranes for Ion Management in (Photo)Electrochemical Energy Conversion. *Accounts Mater. Res.* **2021**, *2* (12), 1156–1166. <https://doi.org/10.1021/accountsmr.1c00113>.
- (9) Simons, R.; Khanarian, G. Water Dissociation in Bipolar Membranes: Experiments and Theory. *J. Membr. Biol.* **1978**, *38* (1–2), 11–30. <https://doi.org/10.1007/BF01875160>.
- (10) Ramírez, P.; Rapp, H.-J.; Mafé, S.; Bauer, B. Bipolar Membranes under Forward and Reverse Bias Conditions. Theory vs. Experiment. *J. Electroanal. Chem.* **1994**, *375* (1–2), 101–108. [https://doi.org/10.1016/0022-0728\(94\)03379-X](https://doi.org/10.1016/0022-0728(94)03379-X).
- (11) McDonald, M. B.; Ardo, S.; Lewis, N. S.; Freund, M. S. Use of Bipolar Membranes for Maintaining Steady-State PH Gradients in Membrane-Supported, Solar-Driven Water Splitting. *ChemSusChem* **2014**, *7* (11), 3021–3027. <https://doi.org/10.1002/cssc.201402288>.
- (12) Vargas-Barbosa, N. M.; Geise, G. M.; Hickner, M. A.; Mallouk, T. E. Assessing the Utility of Bipolar Membranes for Use in Photoelectrochemical Water-Splitting Cells. *ChemSusChem* **2014**, *7* (11), 3017–3020. <https://doi.org/10.1002/cssc.201402535>.
- (13) Luo, J.; Vermaas, D. A.; Bi, D.; Hagfeldt, A.; Smith, W. A.; Grätzel, M. Bipolar Membrane-Assisted Solar Water Splitting in Optimal PH. *Adv. Energy Mater.* **2016**, *6* (13), 1600100. <https://doi.org/10.1002/aenm.201600100>.

- (14) Mayerhöfer, B.; McLaughlin, D.; Böhm, T.; Hegelheimer, M.; Seeberger, D.; Thiele, S. Bipolar Membrane Electrode Assemblies for Water Electrolysis. *ACS Appl. Energy Mater.* **2020**, *3* (10), 9635–9644. <https://doi.org/10.1021/acsaem.0c01127>.
- (15) Oener, S. Z.; Foster, M. J.; Boettcher, S. W. Accelerating Water Dissociation in Bipolar Membranes and for Electrocatalysis. *Science*. **2020**, *369* (6507), 1099–1103. <https://doi.org/10.1126/science.aaz1487>.
- (16) Oener, S. Z.; Twright, L. P.; Lindquist, G. A.; Boettcher, S. W. Thin Cation-Exchange Layers Enable High-Current-Density Bipolar Membrane Electrolyzers via Improved Water Transport. *ACS Energy Lett.* **2021**, *6* (1), 1–8. <https://doi.org/10.1021/acsenenergylett.0c02078>.
- (17) Vermaas, D. A.; Smith, W. A. Synergistic Electrochemical CO₂ Reduction and Water Oxidation with a Bipolar Membrane. *ACS Energy Lett.* **2016**, *1* (6), 1143–1148. <https://doi.org/10.1021/acsenenergylett.6b00557>.
- (18) Li, Y. C.; Zhou, D.; Yan, Z.; Gonçalves, R. H.; Salvatore, D. A.; Berlinguette, C. P.; Mallouk, T. E. Electrolysis of CO₂ to Syngas in Bipolar Membrane-Based Electrochemical Cells. *ACS Energy Lett.* **2016**, *1* (6), 1149–1153. <https://doi.org/10.1021/acsenenergylett.6b00475>.
- (19) Zhou, X.; Liu, R.; Sun, K.; Chen, Y.; Verlage, E.; Francis, S. A.; Lewis, N. S.; Xiang, C. Solar-Driven Reduction of 1 Atm of CO₂ to Formate at 10% Energy-Conversion Efficiency by Use of a TiO₂-Protected III–V Tandem Photoanode in Conjunction with a Bipolar Membrane and a Pd/C Cathode. *ACS Energy Lett.* **2016**, *1* (4), 764–770. <https://doi.org/10.1021/acsenenergylett.6b00317>.
- (20) Salvatore, D. A.; Weekes, D. M.; He, J.; Dettelbach, K. E.; Li, Y. C.; Mallouk, T. E.; Berlinguette, C. P. Electrolysis of Gaseous CO₂ to CO in a Flow Cell with a Bipolar Membrane. *ACS Energy Lett.* **2018**, *3* (1), 149–154. <https://doi.org/10.1021/acsenenergylett.7b01017>.
- (21) Pătru, A.; Binninger, T.; Pribyl, B.; Schmidt, T. J. Design Principles of Bipolar Electrochemical Co-Electrolysis Cells for Efficient Reduction of Carbon Dioxide from Gas Phase at Low Temperature. *J. Electrochem. Soc.* **2019**, *166* (2), F34–F43. <https://doi.org/10.1149/2.1221816jes>.
- (22) Blommaert, M. A.; Sharifian, R.; Shah, N.; Nesbitt, N.; Smith, W.; Vermaas, D. A. Orientation of Bipolar Membrane Determines the Dominant Ion and Carbonic Species Transport in Membrane Electrode Assemblies for CO₂ Reduction. *J. Mater. Chem. A* **2021**. <https://doi.org/10.1039/D0TA12398F>.
- (23) Siritanaratkul, B.; Forster, M.; Greenwell, F.; Sharma, P. K.; Yu, E. H.; Cowan, A. J. Zero-Gap Bipolar Membrane Electrolyzer for Carbon Dioxide Reduction Using Acid-Tolerant Molecular Electrocatalysts. *J. Am. Chem. Soc.* **2022**, *144* (17), 7551–7556. <https://doi.org/10.1021/jacs.1c13024>.
- (24) Xie, K.; Miao, R. K.; Ozden, A.; Liu, S.; Chen, Z.; Dinh, C.; Huang, J. E.; Xu, Q.; Gabardo, C. M.; Lee, G.; Edwards, J. P.; O'Brien, C. P.; Boettcher, S. W.; Sinton, D.; Sargent, E. H. Bipolar Membrane Electrolyzers Enable High Single-Pass CO₂ Electroreduction to Multicarbon Products. *Nat. Commun.* **2022**, *13* (1), 3609. <https://doi.org/10.1038/s41467-022-31295-3>.
- (25) Sullivan, I.; Goryachev, A.; Digdaya, I. A.; Li, X.; Atwater, H. A.; Vermaas, D. A.;

- Xiang, C. Coupling Electrochemical CO₂ Conversion with CO₂ Capture. *Nat. Catal.* **2021**, *4* (11), 952–958. <https://doi.org/10.1038/s41929-021-00699-7>.
- (26) Sharifian, R.; Wagterveld, R. M.; Digdaya, I. A.; Xiang, C.; Vermaas, D. A. Electrochemical Carbon Dioxide Capture to Close the Carbon Cycle. *Energy Environ. Sci.* **2021**, *14* (2), 781–814. <https://doi.org/10.1039/D0EE03382K>.
- (27) Ding, Y.; Cai, P.; Wen, Z. Electrochemical Neutralization Energy: From Concept to Devices. *Chem. Soc. Rev.* **2021**, *50* (3), 1495–1511. <https://doi.org/10.1039/D0CS01239D>.
- (28) Zeng, T.-Y.; Xia, L.; Zhang, Z.; Hong, C.-Y.; You, Y.-Z. Dithiocarbamate-Mediated Controlled Copolymerization of Ethylene with Cyclic Ketene Acetals towards Polyethylene-Based Degradable Copolymers. *Polym. Chem.* **2021**, *12* (2), 165–171. <https://doi.org/10.1039/D0PY00200C>.
- (29) Yan, Z.; Wycisk, R. J.; Metlay, A. S.; Xiao, L.; Yoon, Y.; Pintauro, P. N.; Mallouk, T. E. High-Voltage Aqueous Redox Flow Batteries Enabled by Catalyzed Water Dissociation and Acid–Base Neutralization in Bipolar Membranes. *ACS Cent. Sci.* **2021**, *7* (6), 1028–1035. <https://doi.org/10.1021/acscentsci.1c00217>.
- (30) Metlay, A. S.; Chyi, B.; Yoon, Y.; Wycisk, R. J.; Pintauro, P. N.; Mallouk, T. E. Three-Chamber Design for Aqueous Acid–Base Redox Flow Batteries. *ACS Energy Lett.* **2022**, *7* (3), 908–913. <https://doi.org/10.1021/acsendergylett.2c00040>.
- (31) Pärnamäe, R.; Gurreri, L.; Post, J.; van Egmond, W. J.; Culcasi, A.; Saakes, M.; Cen, J.; Goosen, E.; Tamburini, A.; Vermaas, D. A.; Tedesco, M. The Acid–Base Flow Battery: Sustainable Energy Storage via Reversible Water Dissociation with Bipolar Membranes. *Membranes (Basel)*. **2020**, *10* (12), 409. <https://doi.org/10.3390/membranes10120409>.
- (32) Al-Dhubhani, E.; Pärnamäe, R.; Post, J. W.; Saakes, M.; Tedesco, M. Performance of Five Commercial Bipolar Membranes under Forward and Reverse Bias Conditions for Acid-Base Flow Battery Applications. *J. Memb. Sci.* **2021**, *7*, 119748. <https://doi.org/10.1016/j.memsci.2021.119748>.
- (33) Bui, J. C.; Digdaya, I.; Xiang, C.; Bell, A. T.; Weber, A. Z. Understanding Multi-Ion Transport Mechanisms in Bipolar Membranes. *ACS Appl. Mater. Interfaces* **2020**, *12* (47), 52509–52526. <https://doi.org/10.1021/acsam.0c12686>.
- (34) Mitchell, J. B.; Chen, L.; Langworthy, K.; Fabrizio, K.; Boettcher, S. W. Catalytic Proton–Hydroxide Recombination for Forward-Bias Bipolar Membranes. *ACS Energy Lett.* **2022**, *7* (11), 3967–3973. <https://doi.org/10.1021/acsendergylett.2c02043>.
- (35) Sokirko, A. V.; Ramírez, P.; Manzanares, J. A.; Mafés, S. Modeling of Forward and Reverse Bias Conditions in Bipolar Membranes. *Berichte der Bunsengesellschaft für Phys. Chemie* **1993**, *97* (8), 1040–1048. <https://doi.org/10.1002/bbpc.19930970814>.
- (36) Ziv, N.; Mustain, W. E.; Dekel, D. R. The Effect of Ambient Carbon Dioxide on Anion-Exchange Membrane Fuel Cells. *ChemSusChem* **2018**, *11* (7), 1136–1150. <https://doi.org/10.1002/cssc.201702330>.
- (37) Lee, M.-Y.; Park, K. T.; Lee, W.; Lim, H.; Kwon, Y.; Kang, S. Current Achievements and the Future Direction of Electrochemical CO₂ Reduction: A Short Review. *Crit. Rev. Environ. Sci. Technol.* **2020**, *50* (8), 769–815.

<https://doi.org/10.1080/10643389.2019.1631991>.

- (38) Dinh, H. Q.; Toh, W. L.; Chu, A. T.; Surendranath, Y. Neutralization Short-Circuiting with Weak Electrolytes Erodes the Efficiency of Bipolar Membranes. *ACS Appl. Mater. Interfaces* **2023**, *15* (3), 4001–4010. <https://doi.org/10.1021/acsami.2c18685>.
- (39) Vermaas, D. A.; Wiegman, S.; Nagaki, T.; Smith, W. A. Ion Transport Mechanisms in Bipolar Membranes for (Photo)Electrochemical Water Splitting. *Sustain. Energy Fuels* **2018**, *2* (9), 2006–2015. <https://doi.org/10.1039/C8SE00118A>.
- (40) Haynes, W. M.; Lide, D. R.; Bruno, T. J. *CRC Handbook of Chemistry and Physics*, 97th ed.; CRC Press, 2016. <https://doi.org/10.1201/9781315380476>.
- (41) Grew, K. N.; McClure, J. P.; Chu, D.; Kohl, P. A.; Ahlfield, J. M. Understanding Transport at the Acid-Alkaline Interface of Bipolar Membranes. *J. Electrochem. Soc.* **2016**, *163* (14), F1572–F1587. <https://doi.org/10.1149/2.0941614jes>.
- (42) Marioni, N.; Zhang, Z.; Zofchak, E. S.; Sachar, H. S.; Kadulkar, S.; Freeman, B. D.; Ganesan, V. Impact of Ion–Ion Correlated Motion on Salt Transport in Solvated Ion Exchange Membranes. *ACS Macro Lett.* **2022**, *11* (11), 1258–1264. <https://doi.org/10.1021/acsmacrolett.2c00361>.
- (43) Ünlü, M.; Zhou, J.; Kohl, P. A. Hybrid Anion and Proton Exchange Membrane Fuel Cells. *J. Phys. Chem. C* **2009**, *113* (26), 11416–11423. <https://doi.org/10.1021/jp903252u>.
- (44) Daud, S. S.; Norrdin, M. A.; Jaafar, J.; Sudirman, R. The Effect of Material on Bipolar Membrane Fuel Cell Performance: A Review. *IOP Conf. Ser. Mater. Sci. Eng.* **2020**, *736* (3), 032003. <https://doi.org/10.1088/1757-899X/736/3/032003>.
- (45) Bard, A. J.; Faulkner, L. R. *Electrochemical Methods: Fundamentals and Applications*, 2nd ed.; John Wiley & Sons: New York, 2001. <https://doi.org/10.1016/B978-0-12-381373-2.00056-9>.
- (46) Chu, S.; Majumdar, A. Opportunities and Challenges for a Sustainable Energy Future. *Nature* **2012**, *488* (7411), 294–303. <https://doi.org/10.1038/nature11475>.
- (47) Chu, S.; Cui, Y.; Liu, N. The Path towards Sustainable Energy. *Nat. Mater.* **2017**, *16* (1), 16–22. <https://doi.org/10.1038/nmat4834>.
- (48) De Luna, P.; Hahn, C.; Higgins, D.; Jaffer, S. A.; Jaramillo, T. F.; Sargent, E. H. What Would It Take for Renewably Powered Electrosynthesis to Displace Petrochemical Processes? *Science*. **2019**, *364* (6438). <https://doi.org/10.1126/science.aav3506>.
- (49) Zhang, Y.-J.; Sethuraman, V.; Michalsky, R.; Peterson, A. A. Competition between CO₂ Reduction and H₂ Evolution on Transition-Metal Electrocatalysts. *ACS Catal.* **2014**, *4* (10), 3742–3748. <https://doi.org/10.1021/cs5012298>.
- (50) Hall, A. S.; Yoon, Y.; Wuttig, A.; Surendranath, Y. Mesostructure-Induced Selectivity in CO₂ Reduction Catalysis. *J. Am. Chem. Soc.* **2015**, *137* (47), 14834–14837. <https://doi.org/10.1021/jacs.5b08259>.
- (51) Wuttig, A.; Yaguchi, M.; Motobayashi, K.; Osawa, M.; Surendranath, Y. Inhibited Proton Transfer Enhances Au-Catalyzed CO₂-to-Fuels Selectivity. *Proc. Natl. Acad. Sci.* **2016**, *113* (32), E4585–E4593. <https://doi.org/10.1073/pnas.1602984113>.

- (52) Ooka, H.; Figueiredo, M. C.; Koper, M. T. M. Competition between Hydrogen Evolution and Carbon Dioxide Reduction on Copper Electrodes in Mildly Acidic Media. *Langmuir* **2017**, *33* (37), 9307–9313. <https://doi.org/10.1021/acs.langmuir.7b00696>.
- (53) Goyal, A.; Marcandalli, G.; Mints, V. A.; Koper, M. T. M. Competition between CO₂ Reduction and Hydrogen Evolution on a Gold Electrode under Well-Defined Mass Transport Conditions. *J. Am. Chem. Soc.* **2020**, *142* (9), 4154–4161. <https://doi.org/10.1021/jacs.9b10061>.
- (54) Rabinowitz, J. A.; Kanan, M. W. The Future of Low-Temperature Carbon Dioxide Electrolysis Depends on Solving One Basic Problem. *Nat. Commun.* **2020**, *11* (1), 5231. <https://doi.org/10.1038/s41467-020-19135-8>.
- (55) Xie, K.; Ozden, A.; Miao, R. K.; Li, Y.; Sinton, D.; Sargent, E. H. Eliminating the Need for Anodic Gas Separation in CO₂ Electroreduction Systems via Liquid-to-Liquid Anodic Upgrading. *Nat. Commun.* **2022**, *13* (1), 3070. <https://doi.org/10.1038/s41467-022-30677-x>.
- (56) Huang, J. E.; Li, F.; Ozden, A.; Sedighian Rasouli, A.; García de Arquer, F. P.; Liu, S.; Zhang, S.; Luo, M.; Wang, X.; Lum, Y.; Xu, Y.; Bertens, K.; Miao, R. K.; Dinh, C.-T.; Sinton, D.; Sargent, E. H. CO₂ Electrolysis to Multicarbon Products in Strong Acid. *Science*. **2021**, *372* (6546), 1074–1078. <https://doi.org/10.1126/science.abg6582>.
- (57) Monteiro, M. C. O.; Philips, M. F.; Schouten, K. J. P.; Koper, M. T. M. Efficiency and Selectivity of CO₂ Reduction to CO on Gold Gas Diffusion Electrodes in Acidic Media. *Nat. Commun.* **2021**, *12* (1), 4943. <https://doi.org/10.1038/s41467-021-24936-6>.
- (58) Pan, B.; Fan, J.; Zhang, J.; Luo, Y.; Shen, C.; Wang, C.; Wang, Y.; Li, Y. Close to 90% Single-Pass Conversion Efficiency for CO₂ Electroreduction in an Acid-Fed Membrane Electrode Assembly. *ACS Energy Lett.* **2022**, 4224–4231. <https://doi.org/10.1021/acsenergylett.2c02292>.
- (59) Li, J.; Kornienko, N. Electrocatalytic Carbon Dioxide Reduction in Acid. *Chem Catal.* **2022**, *2* (1), 29–38. <https://doi.org/10.1016/j.cheecat.2021.10.016>.
- (60) Gu, J.; Liu, S.; Ni, W.; Ren, W.; Haussener, S.; Hu, X. Modulating Electric Field Distribution by Alkali Cations for CO₂ Electroreduction in Strongly Acidic Medium. *Nat. Catal.* **2022**, *5* (4), 268–276. <https://doi.org/10.1038/s41929-022-00761-y>.
- (61) Qiao, Y.; Lai, W.; Huang, K.; Yu, T.; Wang, Q.; Gao, L.; Yang, Z.; Ma, Z.; Sun, T.; Liu, M.; Lian, C.; Huang, H. Engineering the Local Microenvironment over Bi Nanosheets for Highly Selective Electrocatalytic Conversion of CO₂ to HCOOH in Strong Acid. *ACS Catal.* **2022**, *12* (4), 2357–2364. <https://doi.org/10.1021/acscatal.1c05135>.
- (62) O’Brien, C. P.; Miao, R. K.; Liu, S.; Xu, Y.; Lee, G.; Robb, A.; Huang, J. E.; Xie, K.; Bertens, K.; Gabardo, C. M.; Edwards, J. P.; Dinh, C.; Sargent, E. H.; Sinton, D. Single Pass CO₂ Conversion Exceeding 85% in the Electrosynthesis of Multicarbon Products via Local CO₂ Regeneration. *ACS Energy Lett.* **2021**, *6* (8), 2952–2959. <https://doi.org/10.1021/acsenergylett.1c01122>.
- (63) Xu, Y.; Miao, R. K.; Edwards, J. P.; Liu, S.; O’Brien, C. P.; Gabardo, C. M.; Fan, M.; Huang, J. E.; Robb, A.; Sargent, E. H.; Sinton, D. A Microchanneled Solid Electrolyte

- for Carbon-Efficient CO₂ Electrolysis. *Joule* **2022**, *6* (6), 1333–1343. <https://doi.org/10.1016/j.joule.2022.04.023>.
- (64) Kim, J. Y. ‘Timothy’; Zhu, P.; Chen, F.-Y.; Wu, Z.-Y.; Cullen, D. A.; Wang, H. Recovering Carbon Losses in CO₂ Electrolysis Using a Solid Electrolyte Reactor. *Nat. Catal.* **2022**, *5* (4), 288–299. <https://doi.org/10.1038/s41929-022-00763-w>.
- (65) Ozden, A.; García de Arquer, F. P.; Huang, J. E.; Wicks, J.; Sisler, J.; Miao, R. K.; O’Brien, C. P.; Lee, G.; Wang, X.; Ip, A. H.; Sargent, E. H.; Sinton, D. Carbon-Efficient Carbon Dioxide Electrolysers. *Nat. Sustain.* **2022**, *5* (7), 563–573. <https://doi.org/10.1038/s41893-022-00879-8>.
- (66) Fan, L.; Xia, C.; Zhu, P.; Lu, Y.; Wang, H. Electrochemical CO₂ Reduction to High-Concentration Pure Formic Acid Solutions in an All-Solid-State Reactor. *Nat. Commun.* **2020**, *11* (1), 3633. <https://doi.org/10.1038/s41467-020-17403-1>.
- (67) Miao, R. K.; Xu, Y.; Ozden, A.; Robb, A.; O’Brien, C. P.; Gabardo, C. M.; Lee, G.; Edwards, J. P.; Huang, J. E.; Fan, M.; Wang, X.; Liu, S.; Yan, Y.; Sargent, E. H.; Sinton, D. Electroosmotic Flow Steers Neutral Products and Enables Concentrated Ethanol Electroproduction from CO₂. *Joule* **2021**, *5* (10), 2742–2753. <https://doi.org/10.1016/j.joule.2021.08.013>.
- (68) Iddya, A.; Zarzycki, P.; Kingsbury, R.; Khor, C. M.; Ma, S.; Wang, J.; Wheeldon, I.; Ren, Z. J.; Hoek, E. M. V.; Jassby, D. A Reverse-Selective Ion Exchange Membrane for the Selective Transport of Phosphates via an Outer-Sphere Complexation–Diffusion Pathway. *Nat. Nanotechnol.* **2022**, *17* (11), 1222–1228. <https://doi.org/10.1038/s41565-022-01209-x>.